International Journal of Academic Engineering Research (IJAER)
ISSN: 2643-9085
Vol. 5 Issue 3, March - 2021, Pages: 67-74

Impact of the Growth Strategy and Device Fabrication on the Alloy Homogeneity in Optoelectronic Grade Sn-Rich GeSn

Jurabek Abdiyev[1],Sadulla Saydullayev[1], Elyor G'aybulloyev[2], Sherzod Yarashev[2*], Bekzod Erkinov[2]

[1]Physical-technical Institute of NPO "Physics – Sun" of Uzbekistan Academy of Sciences Uzbekistan, Tashkent, Chingiz Aitmatov street 2B.

[2]Tashkent University of Information Technologies named after Muhammad al-Khwarizmi, Uzbekistan, Tashkent, Amir Temur street 108.

Corresponding author: sherzodyarashev1997@gmail.com (Sh. Yarashev)

Abstract: *High Sn-content $Ge_{1-x}Sn_x$ alloys are excellent candidates for the fabrication of electronic and optoelectronic monolithically integrated devices on CMOS platforms. The fabrication of high performance devices requires high quality GeSn layers free of Sn precipitates. This work reports on the characterization of GeSn layers and micro-disk lasers with Sn concentrations ranging from 6 to 16% using synchrotron nano X-ray fluorescence mapping and nano X-ray absorption spectroscopy techniques. We demonstrate that the Sn precipitation observed in thick GeSn layers grown directly on Ge buffers can be fully suppressed, for Sn concentrations as high as 16%, with Ge1-xSnx step-graded buffers. The combination of optimal micro-disk fabrication parameters and full suppression of Sn precipitation can explain the superior lasing performance obtained in micro-disk lasers fabricated using such stacks.*

Keywords: GeSn lasers, XRF, XANES, X-ray nanoprobe.

1. INTRODUCTION.

The attractive optical and electrical properties of Ge1-xSnx (GeSn) have resulted in extensive studies on this alloy, aiming to develop de-vices monolithically integrated on existing CMOS platforms for micro-electronic and photonic applications as FINFET or future integrated light sources for chemical and bio-medical sensing. For instance, the incorporation of Sn into a Ge crystalline lattice increases the effective hole mobility of Ge p-type metal–oxide semiconductor field effect transistors and fin field-effect transistors [1,2]. The growth of crystalline Ge1-xSnx reduces the indirect bandgap of Ge and turns the material band gap from indirect to direct for Sn concentrations higher than 6.5% [3]. In such an alloy, the majority of the Sn atoms are in substitutional sites, as expected for an isovalent impurity. However, Sn concentrations exceeding the solid solubility limits of this element into Ge [4] can generate metallic Sn precipitates in relatively low Sn-content layers [5]. Out of equilibrium growth conditions have recently been used to grow crystalline GeSn layers with high Sn contents [6,7,8,9]. However, the large lattice mismatch between Ge and such alloys has proven to be a major limitation for the growth of high quality thick layers. Overcoming these challenges is necessary to improve the optical and electrical performance of this material and thus the performance of the devices based on it.

Having high-quality direct bandgap $Ge_{1-x}Sn_x$ alloys relies in (i) the control of growth conditions to obtain substitutional Sn atoms incorporation into the Ge matrix and (ii) the control of the built-in compressive strain in the GeSn layers during epitaxy. Ge1-xSn x alloys grown below or above their critical thicknesses are subject to various degrees of compressive strain due to the large lattice mismatch between the Ge strain relaxed buffers (SRB) and the GeSn layers (aGe = 5.658 Å ↔aSn = 6.489 Å). Relaxing the built-in strain in GeSn alloys is essential not only to prevent the appearance of structural defects and Sn segregation, but also to lower the Γ-valley (direct bandgap) below the L-valley (indirect bandgap). The use of step-graded buffers (SGB) is one of the strategies used to accommodate most of the built-in strain during the growth of thick layers [8]. On the other hand, the fabrication of quasi-suspended GeSn micro-disks enables to (i) relax the residual strain in the GeSn layers and (ii) confine its optical modes [10,11,12,13]. These two approaches yielded excellent lasing performances in micro-disk lasers operating at temperatures as high as 230 K [12,13]. However, the impact that buffer and micro-disks fabrication processes have on lasing is still unclear. Understanding the dependence of the local Sn environment on these two parameters would help to further improve the quality of GeSn layers and the performance of these optoelectronic devices.

In previous works, the local Sn environment in pseudo orphic GeSn layers has been studied by Extended X-ray absorption fine structure (EXAFS) measurements [5,14,15]. Furthermore, X-ray diffraction (XRD) and Rutherford backscattering (RBS) enabled to complement those studies in the long-range order regime [16,17,18]. In this study, we have performed for the first time nano X-ray Fluorescence (XRF) mapping and nano X-ray Absorption Near Edge Structure (XANES) measurements on micro-disk lasers with thick GeSn active layers grown on Ge SRBs and Ge1-xSnx SGBs. Nano-XRF enables to measure the elemental distribution and the alloy homogeneity of these micro-disks with a lateral spatial resolution of 50 nm. On the other hand, nano-XANES provides information on the local environment of Sn into the different GeSn layers, with a lateral resolution better than 100 nm.

2. MATERIAL AND METHODS.

The Ge Strain-relaxed Buffers used as templates for GeSn epitaxy were grown with GeH4 using a low temperature/high temperature approach and some short duration thermal cycling under H2 afterwards. Those Ge SRBs were smooth and slightly tensile strained, with a typical threading dislocations density of around 10^7 cm^{-2} [19]. The growth of $Ge_{1-x}Sn_x$ alloys on top of the 1.3 and 2.5 µm thick Ge SRBs has been carried out with Ge_2H_6 + $SnCl_4$ in a dedicated Reduced Pressure - Chemical Vapor Deposition chamber. The growth pressure was 100 Torr, while the temperature was in the 300 ° C – 350 °C range. Higher Sn content layers were grown thanks to a lowering of the temperature in that range, as explained in reference [20]. Several configurations with indirect and direct band-gaps have been grown, with Sn contents ranging from 6% to 16%. It is now accepted that 6–8% is the Sn-concentration for a transition from an indirect to direct band gap in a strain free GeSn layer [21]. Four layers have been grown to evaluate the local environment around the Sn atoms for different concentration and thicknesses regimes. Table 1 gives the Ge buffer and layer thicknesses, as well as the Sn concentration of the GeSn layers. The first three layers (samples 8, 9 and 10) have thicknesses and Sn concentrations expected to produce pseudomorphic layers, whereas sample 12 is expected to exhibit Sn segregation due to its thickness beyond the critical one for such a Sn concentration.

Two strategies were explored to grow thick, high Sn content GeSn layers [8]. The first targeted the growth of high Sn-concentration GeSn layers directly on a Ge SRB. In that case, the Sn incorporation, strongly influenced by the material strain [23], changed during the growth process. This created two clearly differentiated layers (sample 2 in Table 2), with a transition layer between them for higher targeted Sn-concentrations (samples 3 and 4 in Table 2). The second strategy used GeSn SGBs to growth on top of it the thick high Sn content GeSn layer of interest (samples 6, 7 and 11 in Table 2). Sample 11 includes a very thin SiGeSn transition layer between the Ge SRB and the first GeSn layer of the SGB.

The GeSn micro-disk lasers were then fabricated using conventional List of GeSn layers characterized with their corresponding Sn composition and thicknesses. The compositions were obtained from nano-Auger or Transmission Electron Microscopy (TEM) Energy Dispersive X-Ray Analysis (EDX) measurements. The thicknesses have been determined by high resolution X-ray diffraction [22]"

Table 1

Sample	Ge SRB thickness (µm)	Thickness (nm)	Sn content (%)
8	1.3	60	10
9	1.3	54	13
10	1.3	31	16
12	2.5	480	16

List of micro-disks characterized with their corresponding (sub-)layers composition and thicknesses. Compositions were obtained from nano-Auger or TEM EDX measurements. The thicknesses have been measured by a combination of Scanning Electron Microscope in a cross section configuration and TEM EDX [8].

Table 2

Sample	Ge SRB thickness (µm)	Thickness (nm)	Sn content (%)
2	2.5	200	7
		200	8
3	2.5	120	10 (bottom)
		90	Transit. layer
		220	12 (top)
4	2.5	160	13 (bottom)
		60	Transit. layer
		210	16 (top)
6	1.3	120	6 (bottom)
		120	8
		240	11 (top)
7	1.3	120	8 (bottom)
		112	10
		108	12
		181	16 (top)
11	2.5	30	SiGeSn layer
		120	6 (bottom)
		120	8
		120	10
		240	14
		120	11 (top)

	30	SiGeSn layer

lithography and etching steps in thick and high Sn content GeSn layers. Electron beam lithography was first performed using a negative tone ma-N 2410 resist to define the micro-disks area. Anisotropic etching was then carried out in an Inductively Coupled Plasma-Reactive Ion Etching reactor with a Cl2 chemistry, until the Ge/GeSn interface was reached. The etching mode was then switched from anisotropic to isotropic (pure ICP mode) and the gas changed to a CF4 based mixture [24,25]. In this regime, Ge was selectively etched with respect to GeSn, resulting in the formation of GeSn micro-disks on Ge pedestals (Fig. 1). The Ge pedestal diameter was finely tuned by changing the etching time. Finally, the remaining resist on top of the micro-disk was plasma etched with oxy-gen. Fig. 1 shows a micro-disk fabricated with the GeSn step-graded buffer strategy. Different diameter micro-disks were fabricated, with diameters ranging from 6 up to 20 µm. Micro-disks were along lines at 45◦from the silicon ⟨110⟩ cleaving directions. In this configuration, cleaving a processed sample in the middle of the lithographic field enabled us to observe a single micro-disk close to the cleaving edge, without any other disk in the field of view.

Taking advantage of the hard X-ray nanoprobe beamline ID16B at the European Synchrotron Radiation Facility (ESRF) [26], we have performed nano-XRF and nano-XANES measurements on the full set of samples listed in Table 1 and Table 2. The nano-XRF measurements were performed using a 33.8 keV pink beam ($4x10^{10}$ ph/s, E/E ≈ 10^{-2}), whereas the nano-XANES measurements were done with a mono-chromatic beam ($6x10^{8}$ ph/s, E/E ≈ 10^{-4}). Multilayer Kirkpatrick Baez mirrors focused the X-ray beam down to 51 × 60 nm^2 (HxV) in pink mode, and 88 × 66 nm^2 (HxV) in monochromatic mode (See Figure S1 in the Suppl. Info). Six large area (50 mm^2) silicon drift detectors detected the XRF signal emitted by the sample during XRF and XANES measurements.

XANES measurements around the K-edge (probing 1 s electrons) were performed in fluorescence mode over an energy range of 350 eV (100 eV below and 250 eV above the K absorption edge), using 1 eV steps with 200 ms accumulation per point. Several XANES spectra were acquired on each studied area to improve the signal to noise ratio. Several spectra taken for each sample were compared to discard any radiation-induced modification of the sample. The position of the sample was verified before each new scan to correct any vertical shift of the beam due to the non-perfect repositioning of the monochromator, or any possible shift of the sample. XANES data processing and analysis was performed using the ATHENA utility [27].

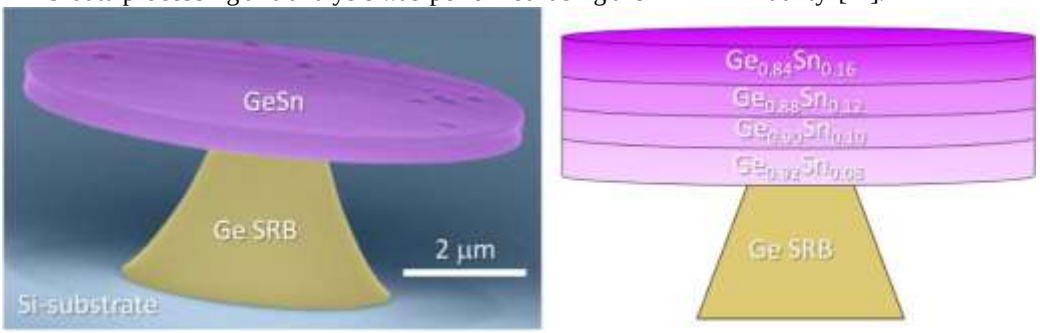

Fig. 1. Scanning electron microscope tilted view image of a micro-disk laser (left). Cross-section schematics of micro-disk 7 described in Table 2 (Right).

3. RESULTS AND DISCUSSION.

GeSn micro-disks were scanned using XRF to examine the compositional homogeneity with a pixel size of 50x50 nm^2 and an accumulation time of 300 ms per pixel. Fitting the XRF spectra using the PyMca software [28] provided the intensity of each XRF line for each element present in the sample and for each pixel. This enabled us to plot this intensity to obtain elemental distribution maps over the studied area.

Fig. 2 shows the Sn- K_α, Ge- K_α and Sn- K_α/Ge K_α XRF lines intensity maps of the full set of micro-disks. The alloy composition of the first layer after the SRB is given on top of each column. The intensity scale of the maps has been selected to have the central region (with higher intensity due to the Ge pedestal XRF and scattering) saturated, increasing the contrast at the outer region of the micro-disks. The pedestals have truncated conical shapes with a circular cross section at the bottom and a square cross section at the top as evidenced in the Ge-K_α and Sn-K_α XRF maps, respectively. The small differences in the size of the pedestals is due to slightly different etching times used during the fabrication of the various micro-disks.

The Sn-K_α XRF intensity maps show an almost constant intensity over the entire micro-disk, with very smooth modulations of the intensity, more pronounced in the case of Sample 2. The Ge- K_α maps show three distinctive features: *i*) well-defined random pattern (disks 2, 6 and 7); *ii*) constant XRF intensity and rounded higher intensity/thicker regions (disks 3 and 4); *iii*) and constant XRF intensity and rounded lower intensity/thinner regions (disk 11). The Sn/Ge K_α ratio maps show more clearly the difference between the three types of features and help to identify their origin. Thicker rounded regions in disks 3 and 4 are not observed in the ratio maps, indicating that they are not Sn or Ge precipitates but Ge1-xSnx alloy, instead. Scanning Electron Microscope (SEM) images show these rounded thicker regions are at the top of the micro-disks (Figure S2 – Suppl. Info). By contrast, the

thinner rounded regions in micro-disk 11 are observed as higher intensity spots in the ratio map, indicating they are likely due to a local removal of Ge during the etching process. SEM images of micro-disk 11 (Figure S2 – Suppl. Info) shows a flat top surface, therefore these regions should be at the bottom surface. Finally, the random patterns in the ratio maps are an inverse image of those in the Ge maps, and are located at the bottom surface (Figure S2 – Suppl. Info). This pattern should come from a partial inhomogeneous etching of the first Ge1-xSnx layer during the micro-disk lasers fabrication. The undesired etching is observed only when the first layer has a Sn-concentration ≤ 8% (micro-disks 2, 6 and 7), but can be avoided by adding a thin SiGeSn layer (micro-disks 11). Higher Sn-concentrations in the first layer would increase its mismatch with the Ge-buffer and its strain, and thus the number of defects at the interface that can propagate into the Ge1-xSnx stack. Therefore, the best strategy to avoid the undesired etching of the first SGB layer is the growth of an intermediary thin SiGeSn layer.

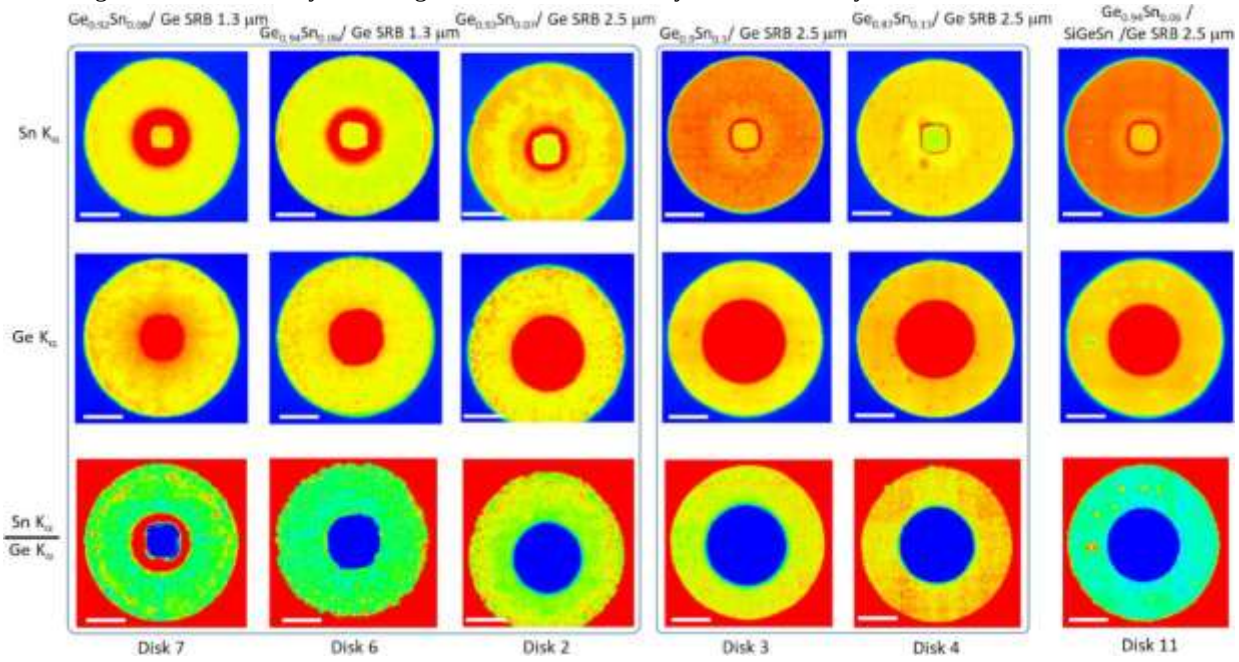

Fig. 2. XRF maps of the entire set of studied micro-disk lasers arranged by columns. From top to bottom, Sn-K_α, Ge-K_α, and Sn/Ge K_α XRF lines intensity ratio. The alloy composition of the first layer in the stack is given on top of each column. The scale bar corresponds to 2 µm.

From the XRF analysis it is not possible to clarify if there are tiny metallic Sn-precipitates in the GeSn layers, generated either during the epitaxy or the fabrication of the micro-disk lasers. In order to clarify this question, we have performed nano-XANES measurements around the Sn K-edge. First, the three thin Ge1-xSnx layers listed in Table 1 along with a metallic Sn foil were characterized. Similarly, XANES measurements around the Ge K-edge was performed on a 1.5 µm thick Ge SRB and on bulk monocrystalline Ge. These results are shown in Fig. 3. Ge SRB and bulk Ge exhibited the same well defined features above the absorption edge over the whole scanned energy. The Sn K-edge XANES of the three layers nicely reproduced the main features of the Ge K-edge, although they were less pronounced. This showed that Sn atoms incorporated in substitutional sites of the Ge lattice. The less pronounced features observed in the XANES of alloy layers can be due to a worse energy resolution at high energy and to the intrinsic disorder of the alloy. The second possibility is reinforced by a more pronounced broadening observed in the layer with a higher Sn concentration. Comparing the XANES of the Sn foil with those of the layers, the most distinctive features of the metallic phase (marked with asterisks in the bottom figure) are absent in the layers. These would indicate that the layers are free of metallic Sn precipitates in a short-range order regime. The lack of metallic Sn in the layers was also confirmed by XRD measurements (Figure S3 – Suppl. Info). Therefore, the XANES spectra of these thin layers can be used as standards of metallic Sn-free Ge1-xSnx alloys for Sn-concentrations in the range used for the micro-disk lasers.

The effect of the Ge SRB and GeSn SGB on the quality of the micro-disks layers was studied by XANES. These XANES measurements required a special sample alignment to obtain independent XANES spectra for layers with different Sn concentrations. The micro-disks were mounted with their surface parallel to the X-ray beam. Figure S4 in the Supplementary Info shows the geometry and explains the alignment procedure used for all the micro-disk lasers characterized.

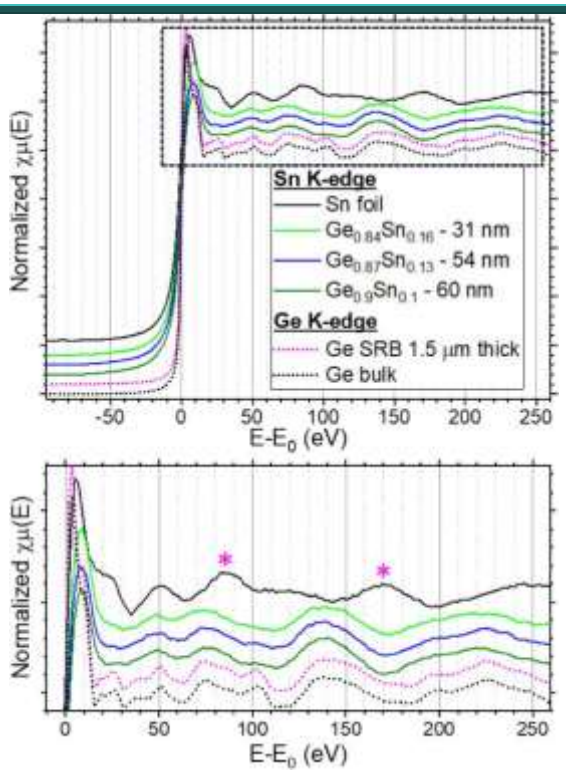

Fig. 3. Top panel shows from top to bottom, Sn K-edge XANES spectra of a 2.5 μm thick tin foil, and those of layers 8, 9 and 10 listed in Table 1, respectively (solid lines). At the bottom, Ge K-edge XANES of two Ge reference samples: 1.5 μm thick Ge SRB on Si and monocrystalline bulk Ge (dashed lines). The zero in the energy axis corresponds to the respective absorption K-edges: 29200 eV for Sn and 11103 eV for Ge. The bottom panel shows a zoom of the region enclosed in the upper panel to facilitate comparison of the oscillations in the spectra.

Fig. 4 shows the Sn K-edge XANES spectra acquired for the top (Sn-richest) Ge1-xSnx layers of the micro-disk lasers 2, 3 and 4 (SRB), 6 and 7 (SGB). XANES spectra of sample 8, Sn metallic foil and sample 12 (480 nm thick Ge0.9Sn0.1 layer) are included for comparison. Sample 12 shows clear signatures of Sn metallic precipitates on its surface, as confirmed by the SEM images (Figure S5 - Supplementary Info). The XANES spectrum of sample 12 shows features observed in the XANES spectra of both the Sn foil and the thin Ge0.9Sn0.1 layer. This confirms the existence of Sn metallic precipitates within the layer. The XANES spectra of the micro-disks reproduce very well that of the Ge 0.9Sn0.1 layer. The distinctive features of the metallic phase (marked with asterisks in Figs. 3 and 4) are not present anymore. However, the features and oscillations in the XANES spectra of the micro-disks are more attenuated and broader than those in the layer spectrum, making it difficult to conclude from a simple visual comparison.

In order to elucidate and ideally quantify the amount of metallic Sn into the various micro-disks layers, Linear Combination Fitting (LCF) has been performed to the XANES spectra measured on bottom and top layers. For the LCF, XANES spectra of the Sn metallic foil and the 31 nm-thick Ge0.84Sn0.16 layer were used as standards. Fig. 5 shows the LCF of the XANES spectra acquired on the bottom and top layers of micro-disks 4 (SRB) and 7 (SGB). The XANES spectra and LCF of the missing samples are shown in Figure S6 of the Suppl. Info. XANES spectra of the bottom layer of micro-disk 2 could not be acquired, most likely due to the inhomogeneous bottom surface generated by the etching process during the micro-disks fabrication. A very good fitting was obtained for the entire set of XANES spectra from the micro-disks. The LCF of sample 12 was not as good as those of the micro-disks. This could indicate the presence of a third phase in sample 12 apart from substitutional and metallic tin.

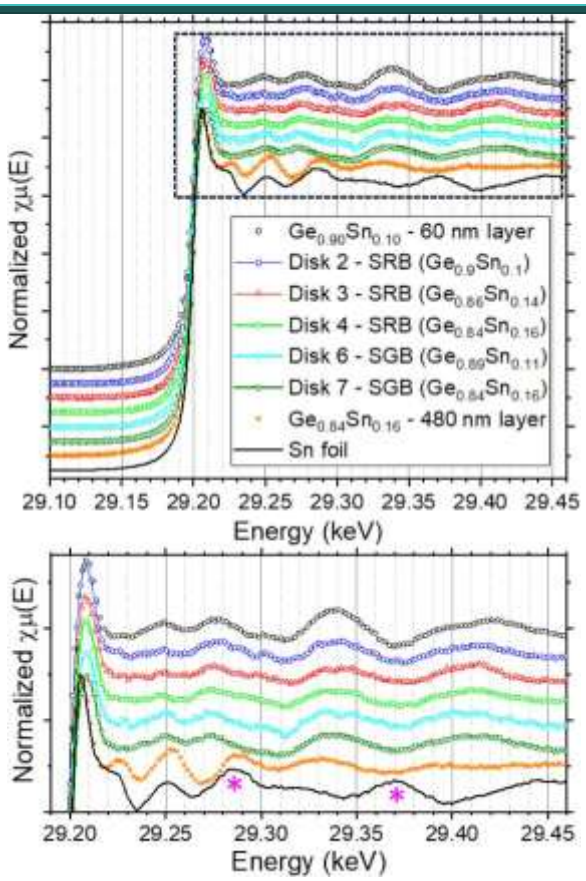

Fig. 4. Top panel shows from top to bottom the Sn K-edge XANES spectra of: sample 8 (60 nm-thick Ge 0.9Sn0.1 layer); top Ge1-xSnx layer of micro-disk lasers 2, 3 and 4 (SRB), 6 and 7 (SGB); layer 12 (480 nm-thick Ge0.84Sn0.16) and a Sn metallic foil. The bottom panel shows a zoom of the region enclosed in the upper panel to facilitate the comparison of the oscillations in the spectra.

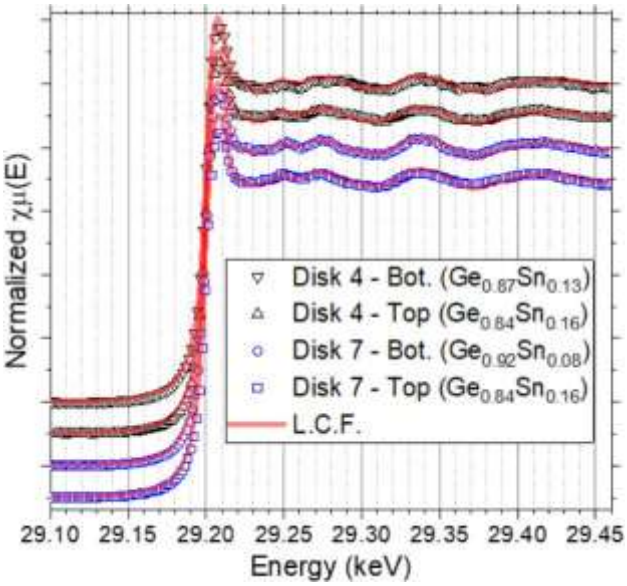

Fig. 5. Linear combination fitting of XANES spectra acquired on the bottom and top layers of micro-disks 4 (SRB) and 7 (SGB).

Table 3 summarizes the ratios of substitutional and metallic Sn along with the corresponding R-factors obtained from the LCF. The very low R-factors confirm the excellent fitting obtained for the micro-disk lasers. The SRB micro-disks results indicate the existence of small fractions of metallic Sn into the bottom and top layers. Although there is not a clear trend due to the reduced number of samples characterized, it seems that, for SRB micro-disks, the amount of metallic Sn increases with the nominal Sn concentration of the layers. There are no clear differences between the metallic Sn fraction in the bottom and top layers of the

micro-disks, except for micro-disk 4 with a smaller metallic Sn fraction in the top layer. On the other hand, SGB micro-disks can be considered, within error bars, as being free of metallic precipitates in bottom and top layers. Finally, the fraction of metallic Sn in sample 12 is as high as 50%. Although this value could be slightly modified by the existence of a third phase, it confirms the very poor quality of thick (400 nm) high Sn concentration (16%) $Ge_{1-x}Sn_x$ layers.

4. CONCLUSION.

In conclusion, we have characterized $Ge_{1-x}Sn_x$ layers and micro-disk lasers with Sn concentrations ranging from 6 to 16%. The fabrication of micro-disks was successfully completed by using electron beam lithography together with plasma etching. XRF mapping showed that there was a partial inhomogeneous etching of the first GeSn layers with Sn concentrations ≤ 8% during the micro-disk lasers' fabrication. The deposition of a thin SiGeSn layer between the GeSn stack and the Ge SRB avoided the undesired etching and enabled to obtain a flat bottom sur-face in the micro-disks. XANES measurements around the Sn K-edge were performed to clarify the effect of the different fabrication conditions on the short-range order of this element inside the micro-disks. The LCF analysis of the XANES spectra confirmed the beneficial impact of using $Ge_{1-x}Sn_x$ SGB, which gradually relaxed the built-in compressive strain, on the quality of the high Sn concentration $Ge_{1-x}Sn_x$ layers on top. The Sn segregation was completely suppressed in thick layers with Sn concentrations as high as 16% (micro-disk 7) by growing on SGB. The Substitutional and metallic Sn percentage obtained from the LCF for the micro-disk lasers and thick layers along with the corresponding R-factor of each fitting.

Table 3

Samples	Layers	Sn content (%)	Sn-substitutional	Sn-metallic	R-factor
2 (SRB)	Top	8	0.92 ± 0.02	0.08 ± 0.02	0.0002
3 (SRB)	Bottom	10	0.91 ± 0.02	0.09 ± 0.02	0.0004
	Top	12	0.89 ± 0.03	0.11 ± 0.03	0.0005
4 (SRB)	Bottom	13	0.83 ± 0.02	0.17 ± 0.02	0.0004
	Top	16	0.89 ± 0.02	0.11 ± 0.02	0.0004
6 (SGB)	Bottom	6	0.98 ± 0.03	0.02 ± 0.03	0.0006
	Top	11	0.96 ± 0.03	0.04 ± 0.03	0.0007
7 (SGB)	Bottom	8	0.98 ± 0.02	0.02 ± 0.02	0.0003
12	Top	16	1.00 ± 0.03	0.0 ± 0.03	0.0006
(SRB)	Top	16	0.50 ± 0.04	0.50 ± 0.04	0.0012

lack of Sn precipitation also indicated that the etching process used to fabricate the micro-disks did not affect the short-range order of Sn into the partially etched Ge lattice. On the other hand, growing the GeSn layers directly on Ge SRB generates the precipitation of a small fraction of Sn in the micro-disk layers for Sn concentrations as low as 8%. The absence of Sn precipitates in the SGB-grown micro-disks explains the superior optoelectronic properties observed in micro-disk lasers fabricated using layers grown on SGB compared with those grown directly on Ge SRB.

REFERENCES

[1] B. Vincent, Y. Shimura, S. Takeuchi, T. Nishimura, G. Eneman, A. Firrincieli, J. Demeulemeester, A. Vantomme, T. Clarysse, O. Nakatsuka, S. Zaima, J. Dekoster, M. Caymax, R. Loo, Microelectron. Eng. 88 (2011) 342.

[2] D. Lei, K.H. Lee, S. Bao, W. Wang, S. Masudy-Panah, S. Yadav, A. Kumar, Y. Dong, Y. Kang, S. Xu, Y. Wu, Y.-C. Huang, H. Chung, S.S. Chu, S. Kuppurao, C.S. Tan, X. Gong, Y.-C. Yeo, Digest of Technical Papers-Symposium on VLSI Technology, no.7998170 (2017).

[3] S. Gupta, B. Magyari-Kope,¨ Y. Nishi, K.C. Saraswat, J. Appl. Phys. 113 (2013), 073707.

[4] F.A. Trumbore, J. Electrochem. Soc. 103 (1956) 597.
[5] E. Kamiyama, K. Sueoka, O. Nakatsuka, N. Taoka, S. Zaima, K. Izunome, K. Kashima, Thin Solid Films 557 (2014) 173.
[6] J. Margetis, S.A. Ghetmiri, W. Du, B.R. Conley, A. Mosleh, R.A. Soref, G. Sun, L. Domulevica, H.A. Naseem, S.-Q. Yu, J. Tolle, ECS Trans. 64 (2014) 711.
[7] G. Grzybowski, R.T. Beeler, L. Jiang, D.J. Smith, J. Kouvetakis, J. Menendez,´ Appl. Phys. Lett. 101 (2012), 072105.
[8] J. Aubin, J.M. Hartmann, A. Gassenq, J.L. Rouviere, E. Robin, V. Delaye, D. Cooper, N. Mollard, V. Reboud, V. Calvo, Semicond. Sci. Techno. 32 (2017).
[9] J. Zheng, Z. Liu, C. Xue, C. Li, Y. Zuo, B. Cheng, Q. Wang, J. Semicond. 39 (2018), 061006.
[10] S. Wirths, R. Geiger, N. von den Driesch, G. Mussler, T. Stoica, S. Mantl, Z. Ikonic, M. Luysberg, S. Chiussi, J.M. Hartmann, H. Sigg, J. Faist, D. Buca, D. Grützmacher, Nat. Photonics 9 (2015) 88.
[11] D. Stange, S. Wirths, R. Geiger, C. Schulte-Braucks, B. Marzban, N. von den Driesch, G. Mussler, T. Zabel, T. Stoica, J.-M. Hartmann, S. Mantl, Z. Ikonic, D. Grützmacher, H. Sigg, J. Witzens, D. Buca, ACS Photonics 3 (2016) 1279.
[12] V. Reboud, A. Gassenq, N. Pauc, J. Aubin, L. Milord, Q.M. Thai, M. Bertrand, K. Guilloy, D. Rouchon, J. Rothman, T. Zabel, F. Armand Pilon, H. Sigg, A. Chelnokov, J.M. Hartmann, V. Calvo, Appl. Phys. Lett. 111 (2017), 092101.
[13] Q.M. Thai, N. Pauc, J. Aubin, M. Bertrand, J. Chretien, V. Delaye, A. Chelnokov, J.-M. Hartmann, V. Reboud, V. Calvo, Opt. Express 26 (2018) 32500.
[14] Y.L. Soo, T.S. Wu, Y.C. Chen, Y.F. Shiu, H.J. Peng, Y.W. Tsai, P.Y. Liao, Y.Z. Zheng, S.L. Chang, T.S. Chan, J.F. Lee, G.E. Sterbinsky, H. Li, H.H. Cheng, Semicond. Sci. Technol. 29 (2014), 115008.
[15] F. Gencarelli, D. Grandjean, Y. Shimura, B. Vincent, D. Banerjee, A. Vantomme, W. Vandervorst, R. Loo, M. Heyns, K. Temst, J. Appl. Phys. 117 (2015), 095702.
[16] F. Gencarelli, B. Vincent, J. Demeulemeester, A. Vantomme, A. Moussa,
[17] A. Franquet, A. Kumar, H. Bender, J. Meersschaut, W. Vandervorst, R. Loo,